Three-dimensional real time imaging of amyloid β aggregation on living cells

SCIENTIFIC REPORTS
nature research

OPEN

Three-dimensional real time imaging of amyloid β aggregation on living cells

Masahiro Kuragano, Ryota Yamashita, Yusaku Chikai, Ryota Kitamura & Kiyotaka Tokuraku✉

Alzheimer's disease (AD) is a progressive disorder of the brain that gradually decreases thinking, memory, and language abilities. The aggregation process of amyloid β (Aβ) is a key step in the expression of its neurocytotoxicity and development of AD because Aβ aggregation and accumulation around neuronal cells induces cell death. However, the molecular mechanism underlying the neurocytotoxicity and cell death by Aβ aggregation has not been clearly elucidated. In this study, we successfully visualized real-time process of $Aβ_{42}$ aggregation around living cells by applying our established QD imaging method. 3D observations using confocal laser microscopy revealed that $Aβ_{42}$ preferentially started to aggregate at the region where membrane protrusions frequently formed. Furthermore, we found that inhibition of actin polymerization using cytochalasin D reduced aggregation of $Aβ_{42}$ on the cell surface. These results indicate that actin polymerization-dependent cell motility is responsible for the promotion of $Aβ_{42}$ aggregation at the cell periphery. 3D observation also revealed that the aggregates around the cell remained in that location even if cell death occurred, implying that amyloid plaques found in the AD brain grew from the debris of dead cells that accumulated $Aβ_{42}$ aggregates.

Alzheimer's disease (AD) is a neurodegenerative disease and progressive disorder of the brain that gradually decreases thinking, memory, and language abilities[1]. The amyloid cascade hypothesis suggests that abnormal aggregation and accumulation of amyloid β (Aβ) causes neurodegeneration in the aged brain[2]. Aβ consists of 39–43 amino acid residues and is derived from amyloid precursor protein that is cleaved by β- and γ-secretase[3]. These short peptides start to aggregate and exhibit neurocytotoxicity[4].

To appreciate the pathological feature of AD, it is important to trace the dynamic behavior of Aβ aggregation to neurons because the aggregation of Aβ is a key step in the development of AD. Several studies on the polymerization and fibrillation of Aβ have been performed using transmission electron microscopy[5–8]. Although high resolution image analysis of $Aβ_{42}$ aggregation is possible, it is necessary to dry the sample for observation. Therefore, observation of Aβ aggregation in a physiological state cannot be performed. Recently, Querol-Vilaseca *et al.* succeeded in the three-dimensional (3D) observation of Aβ present in amyloid plaques of AD patients using stimulated emission depletion microscopy, one type of super resolution microscope[9]. Furthermore, five categories of processes in the aggregation of cellular Aβ were reported using fluorescence-lifetime imaging and 3D structural illumination microscopy[10]. Thus, although the *in situ* analysis of Aβ aggregation is increasing annually, it is difficult to perform the spatiotemporal high resolution analysis of Aβ dynamics under physiological conditions. In particular, the molecular mechanism of interaction between Aβ aggregates and the cell surface has not been clearly elucidated.

It is well known that the interaction between membrane lipids and Aβ is responsible for the modulation of Aβ fibrillation and the expression of neurocytotoxicity[11–13]. The aggregation of Aβ on the cell membrane is an important step in the formation of diffuse plaques[14]. Aβ preferentially accumulated in gangliosides and cholesterol domains of the cell membrane of PC12 cells, and these aggregates exhibited cytotoxicity[15]. Recently, using scanning electron transmission microscopy and an electron tomogram, Han *et al.* reported a 3D interaction between fibrils and the membrane of cells and that fibrils disrupted the membrane and caused leakage of lysosomes[16]. Thus, it has been shown that the cell membrane and its components can function as scaffolds for Aβ aggregation. Moreover, cell membrane morphology and the size of lipid vesicles are also important factors that modulate Aβ aggregation. Sugiura *et al.* reported that Aβ aggregation was enhanced on lipid vesicles displaying high

Graduate School of Engineering, Muroran Institute of Technology, 27-1 Mizumoto, Muroran, 050-8585, Japan. ✉e-mail: tokuraku@mmm.muroran-it.ac.jp

curvature[17]. Small liposomes promoted the formation of Aβ fibrils, whereas huge liposomes inhibited the growth of Aβ fibrils, suggesting that Aβ fibrillation is dependent on liposome size[18]. Diverse morphological changes in the cell membrane are caused by cell motile processes such as cell division and migration, which are physiologically important phenomena. One cytoskeleton protein, actin, plays a particularly important and indispensable role in regulating the morphology of eukaryotic cells. Actin is especially necessary for the formation of filopodia and lamellipodia in motile cells[19]. Actin dynamics, including modulation of its assembly and disassembly, is essential for synaptic plasticity involved with memory skills[20]. Particularly, dynamics of the spine are regulated by the actin cytoskeleton[21]. Small GTPase proteins have important roles in the morphological regulation of neuron cells[20]. Rac1 activity is required for the maintenance of spine shape[22,23]. On the other hand, activation of RhoA exhibits inhibitory function in formation of spines. Overexpression of constitutively active RhoA in hippocampal neurons of mice caused the spine to retract and decrease[24]. Thus, several studies have indicated the importance of the function of actin cytoskeleton in homeostasis of neural tissue. Indeed, F-actin disassembly of the dendritic spine was caused in neuron cells of AD model mice[25]. Aβ affected the architecture of actin and the tubulin network in AD pathology[26]. However, it is obscure whether changes in cell morphology derived from cell motility influence the polymerization and fibrillization of Aβ that exists in culture medium or on the cell membrane. Furthermore, it is unknown whether morphological changes of the cellular membrane, which occur after the formation of actin-dependent protrusions, affect Aβ aggregation in the environment close to the cell surface. This implies that the direct interaction of cell membrane dynamics through actin assembly and Aβ aggregation is also unclear.

Previously, we reported a real-time imaging method of $A\beta_{42}$ aggregation using quantum dot (QD) nanoprobes and developed a microliter-scale high-throughput screening (MSHTS) system for $A\beta_{42}$ aggregation inhibitors that applied this imaging method[27–30]. QD, one of the fluorescent nanoparticle, is a cluster of semiconductor materials composed of hundreds to thousands of selenium and cadmium, and emits fluorescence of various wavelengths according to the particle diameter. Its size is about 10–20 nm, which is almost the same size as the protein. It is known that the advantages of QD are that excitation with a single wavelength light source is possible, and that it is very bright and hardly discolors. Since the extremely high photostability of such QD enables long-term fluorescence observation, it is most suitable for continuous observation of $A\beta_{42}$ aggregation *in vitro*, which progresses on the order of several hours to several days. In MSHTS system, we utilized QD-conjugated $A\beta_{40}$, which had a binding ratio ($A\beta_{40}$/QD) of 6. We synthesized QDAβ by chemically cross-linking QD with NH_2 group attached to the surface and $A\beta_{40}$ with N-terminal cysteine, an amino acid having a thiol group in the side chain. By mixing QDAβ with unlabeled $A\beta_{42}$ at a ratio of 1: 1000, we succeeded in visualizing $A\beta_{42}$ aggregates formed by incubation at 37 °C. These QDAβ were incorporated into $A\beta_{42}$ fibrils with a similar efficiency as unlabeled $A\beta_{42}$. One advantage of this method is that it allows observation of the dynamics of $A\beta_{42}$ aggregation under physiological conditions, which has been difficult until now.

In this study, we succeeded in visualizing the process of $A\beta_{42}$ aggregation with living cells by applying the QD imaging method in real time. In other words, 2D fluorescence microscopy confirmed $A\beta_{42}$ aggregation imaging method by QDAβ are utilized in culture medium. Further, 3D real-time observations using confocal laser microscopy revealed that $A\beta_{42}$ preferentially started to aggregate on the dynamic cell surface where membrane protrusions frequently formed.

Results

Observed $A\beta_{42}$ aggregation around PC12 cells. We initially examined whether $A\beta_{42}$ aggregation was observed in culture medium. Rat adrenal pheochromocytoma PC12 cells, which were differentiated by 4.5 ng/ml nerve growth factor (NGF), were then incubated with 20 μM $A\beta_{42}$ and 30 nM QDAβ for 24 h. After incubation, we observed $A\beta_{42}$ aggregates using a conventional fluorescence microscope (Supplementary Fig. S1) and confocal laser microscope (Fig. 1A). These observations showed that $A\beta_{42}$ aggregates were particularly concentrated around cells. We found cells in which the entire cell periphery was covered by $A\beta_{42}$ aggregates and other cells in which only a part of the cell was covered (Fig. 1B,C). We confirmed that NG108–15 cells from a mouse neuroblastoma × rat glioma hybrid also exhibited $A\beta_{42}$ aggregation at the peripheral region (Supplementary Fig. S2). This indicates that the aggregation of $A\beta_{42}$ is a ubiquitous phenomenon in living cells. Then, we evaluated the neurocytotoxic effects of $A\beta_{42}$ and QD nanoprobes using the 3-(4, 5-dimethylthial-2-yl)-2, 5-diphenyltetrazalium bromide (MTT) assay, and confirmed that the addition of $A\beta_{42}$ reduced cell viability (Supplementary Fig. S3). The combinations of QD or QDAβ and $A\beta_{42}$ also exhibited almost the same result as $A\beta_{42}$ alone. These results indicate that the addition of QDAβ had little effect on the viability of $A\beta_{42}$-treated cells. 3D real-time imaging revealed that early aggregation at the cell periphery occurred after 8 h of incubation (Fig. 2A,B and Supplementary Movies S1 and S2). After 16 h of incubation, there was a dramatic increase in the accumulation of $A\beta_{42}$ aggregates on the cell side. As shown in Fig. 2C, we suggested the model of $A\beta_{42}$ aggregation at the cell periphery. The amount of aggregates increased over time. Interestingly, these 3D observations showed that $A\beta_{42}$ aggregation was not localized on the top of the cell. The amount of $A\beta_{42}$ aggregates surrounding the cell periphery increased over time (Fig. 2D). To clarify the mechanism by which $A\beta_{42}$ binds to cells, cell membranes were stained with a fluorogenic membrane dye, CellBrite green (Fig. 2E). $A\beta_{42}$ and the cell membrane colocalized, indicating that $A\beta_{42}$ might aggregate on the cell surface by specifically interacting with the cell membrane.

Interaction between $A\beta_{42}$ aggregation and protrusive cell membrane. To reveal the process of $A\beta_{42}$ aggregation at the cell's periphery, we performed multi-channel live cell imaging using QDAβ. 2D time lapse observation clarified the formation of $A\beta_{42}$ aggregates with movement of PC12 cell protrusion (Fig. 3A and Supplementary Movie S3). After 24 h of incubation, $A\beta_{42}$ aggregation was observed in the region where membrane protrusions were frequently formed. A kymograph at the edge of the cell showed that $A\beta_{42}$ aggregation first occurred around the protrusions (Fig. 3B, white arrow). Here, we suggested the model of hypotheses that active cell protrusion enhanced $A\beta_{42}$ aggregation (Fig. 3C). In the 3D time lapse observation, the concentration of $A\beta_{42}$

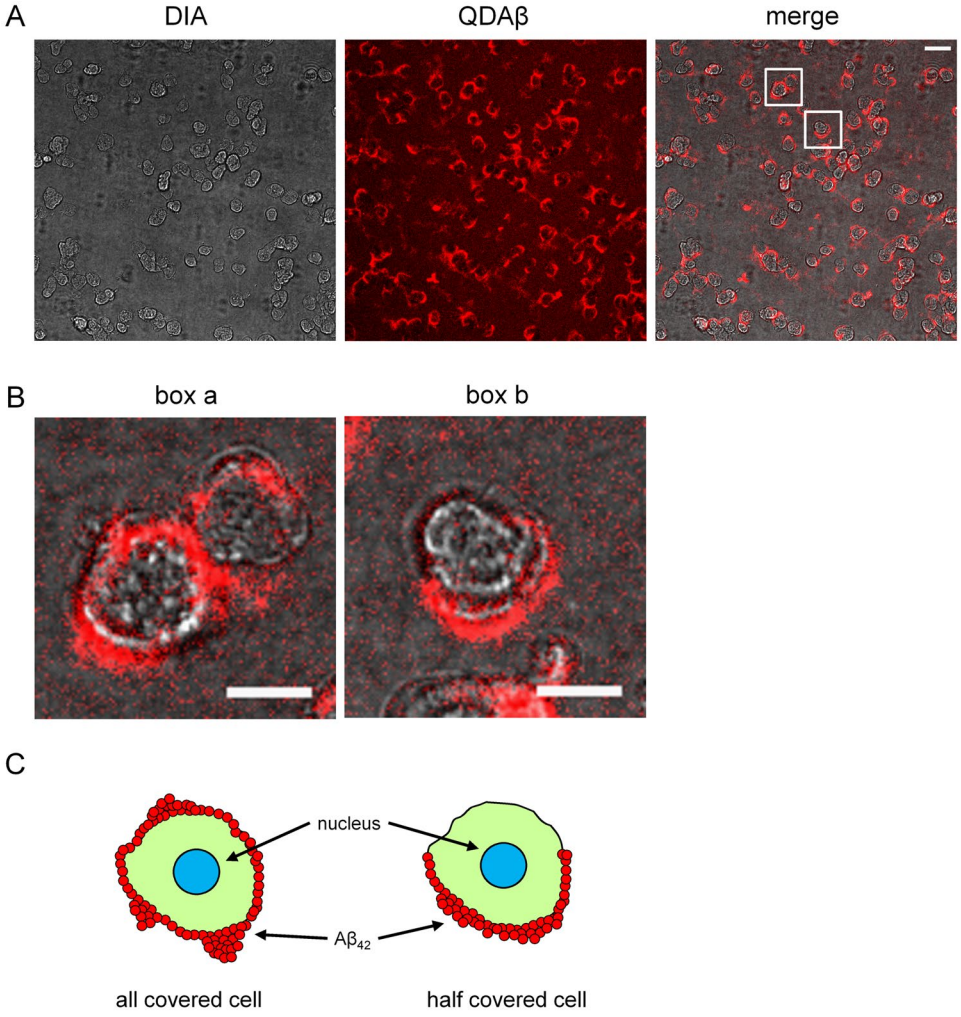

Figure 1. Localization and dynamics of $A\beta_{42}$ aggregation with PC12 cells. (**A**) PC12 cells were co-incubated with 20 μM $A\beta_{42}$ and 30 nM QDAβ, and observed by a conventional inverted microscope (DIA) and a confocal microscope (QDAβ). Bar = 50 μm. (**B**) Magnified images of boxes a and b in panel A. Bar = 20 μm. Cells were covered by $A\beta_{42}$ aggregation on all (box a) or half (box b) of the cell periphery. (**C**) Schematic model of the $A\beta_{42}$ aggregation with PC12 cells.

was reduced to 16 μM to facilitate analysis of $A\beta_{42}$ dynamics on the cell membrane and PC12 cells were transiently transfected to a plasmid with enhanced green fluorescent protein (EGFP) to distinguish cell morphology (Fig. 4). Still images of a maximum fluorescence intensity projection movie showed a time-dependent increase of $A\beta_{42}$ aggregates around the cell (Fig. 4A and Supplementary Movie S4) and the incorporation of $A\beta_{42}$ and QDAβ to intracellular regions by phagocytosis[27]. Furthermore, still images of a 3D reconstruction movie revealed that $A\beta_{42}$ preferentially started to aggregate at the region where membrane protrusions frequently formed (Fig. 4B and Supplementary Movie S5). In Fig. 4C, we suggested 3D model of $A\beta_{42}$ aggregation around the PC12 cell.

To elucidate whether $A\beta_{42}$ aggregations were formed around the cell protrusion specifically, we performed wound healing assay (WHA) with $A\beta_{42}$ and observed $A\beta_{42}$ aggregation processes. WHA is simple and inexpensive method to evaluate the cell motility such as migration rate and directionality[31]. In this method, a confluent cell monolayer was scratched by sharpen tip. Then, it was observed closure process of artificial gap by cell motility. Wu *et al.* reported that PC12 cell showed active protrusions and recovery wounded gap during migration in this assay[32]. As shown in Fig. 5A, we confirmed PC12 cells continued to migrate toward newly created space for 24 h observation. In 24 h time point, PC12 cell exhibited active protrusions (Fig. 5B: white arrows). Incubation with $A\beta_{42}$ and QDAβ during cell migration, we succeeded in observation of preferential formation of $A\beta_{42}$ aggregates at the wounded edge (Fig. 5C and Supplementary Movie S6). To clarify where aggregations were occurred, we analyzed fluorescence intensity profiles along the boxed region in Fig. 5C (+$A\beta_{42}$) and Supplementary Fig. S4 (+DMSO). Fluorescence intensity profiles indicated that $A\beta_{42}$ treated PC12 cells showed characteristic peak around cell edge, suggesting that $A\beta_{42}$ aggregates were formed at the wounded edge (Fig. 5D and Supplementary Fig. S4B). The aggregates showed about 100 μm width across the wounded edge. In other words, $A\beta_{42}$ actively aggregates in the anterior group where cell motility is active (the width of a few cells). We suggested the schematic illustration of preferential aggregation at the wounded edge where frequently protrusions were formed (Fig. 5E).

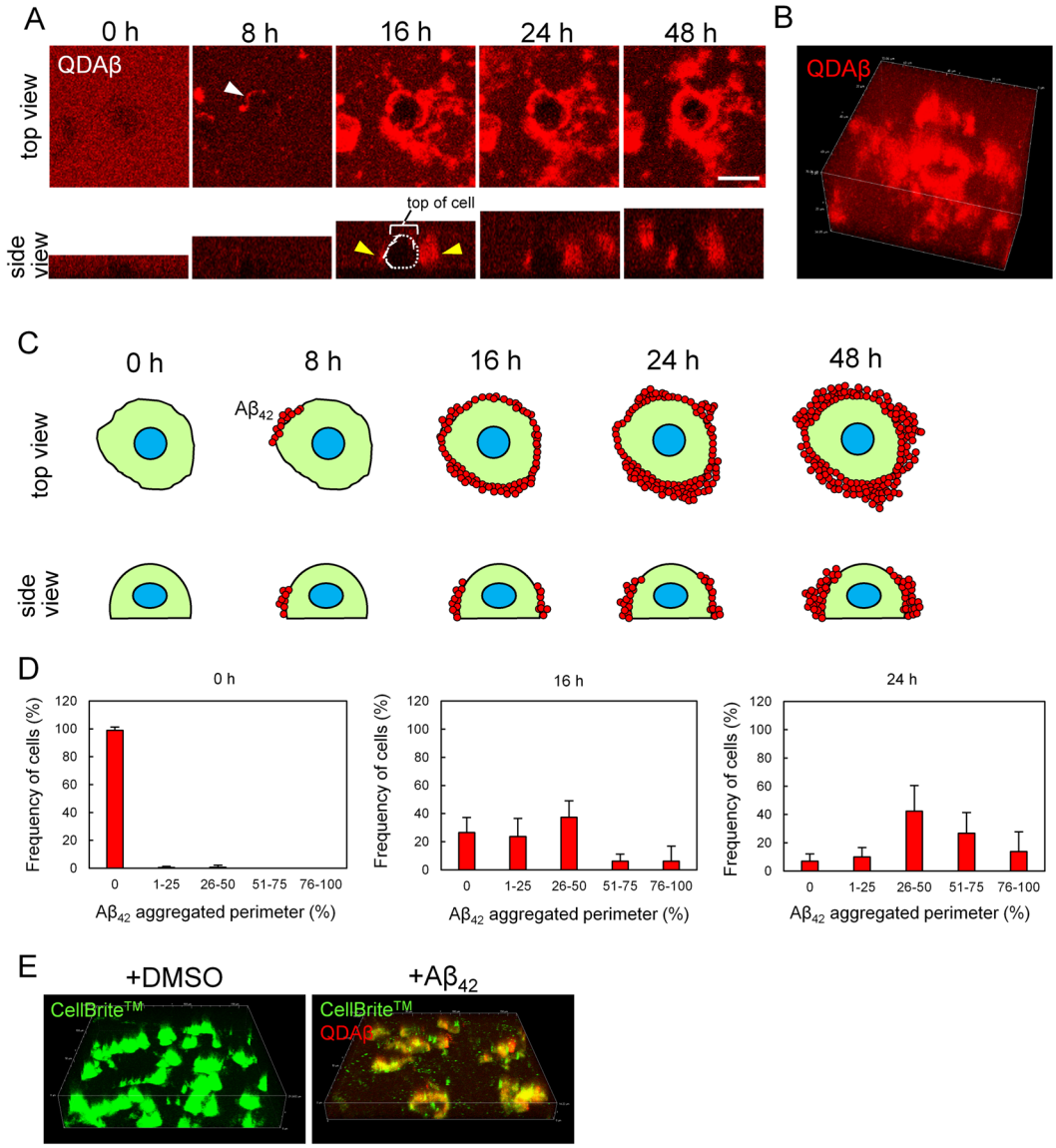

Figure 2. 3D dynamics of $A\beta_{42}$ aggregation with PC12 cells. (**A**) PC12 cells were co-incubated with 20 μM $A\beta_{42}$ and 30 nM QDAβ, and then imaged by confocal microscopy with three-dimensional real-time imaging. White arrowhead indicates early aggregation at 8 h. Approximate cell morphology is shown as dotted lines at 16 h in the side view image. Yellow arrowheads indicate the accumulation of $A\beta_{42}$ aggregates on the cell side. Note that $A\beta_{42}$ aggregation did not localize on top of the cell. Bar = 20 μm. (**B**) 3D reconstruction of 48 h time point in Panel (**A**). (**C**) Schematic model of the $A\beta_{42}$ aggregation around PC12 cells. Top and side view were illustrated. (**D**) Histogram of $A\beta_{42}$ aggregated perimeter (%) after 0, 16, and 24 h incubation. The percentage of $A\beta_{42}$-aggregated perimeter was calculated as the ratio of $A\beta_{42}$-aggregated perimeter to the entire perimeter. n = 470, 268, 235 cells in 0, 16, 24 h incubation, respectively. Error bars represent ±SDs of the mean values of six areas in the well. Note that PC12 cells display time-dependent increase of $A\beta_{42}$ aggregation. (**E**) 3D reconstruction of PC12 co-incubated with 30 μM $A\beta_{42}$ and 30 nM QDAβ. Cells stained with CellBrite green (green). Images were captured by a confocal microscope. Note that $A\beta_{42}$ aggregates (red) colocalized on the cell membrane.

These results demonstrate that active membrane protrusions are essential for the promotion of $A\beta_{42}$ aggregation at the cell periphery.

Observed $A\beta_{42}$ aggregation-induced apoptosis of PC12 cells. The aggregation and accumulation of $A\beta_{42}$ on the surface of a cell membrane have various adverse effects on cellular physiological homeostasis. Actually, human neuroblastoma, SH-SY5Y cells exhibiting the accumulation of $A\beta_{42}$ aggregates undergo apoptosis[33]. As shown in Fig. 6A,B and Supplementary Movie S7, we demonstrated that $A\beta_{42}$ aggregation on the cell surface abruptly caused cell death. Additionally, we found that aggregates of $A\beta_{42}$ cause abnormal cell morphology and the flow of cytoplasmic components out of the cell due to destruction of the cell membrane (Supplementary Fig. S5). Furthermore, we found that $A\beta_{42}$ aggregation led to defects in maintenance of nuclear morphology

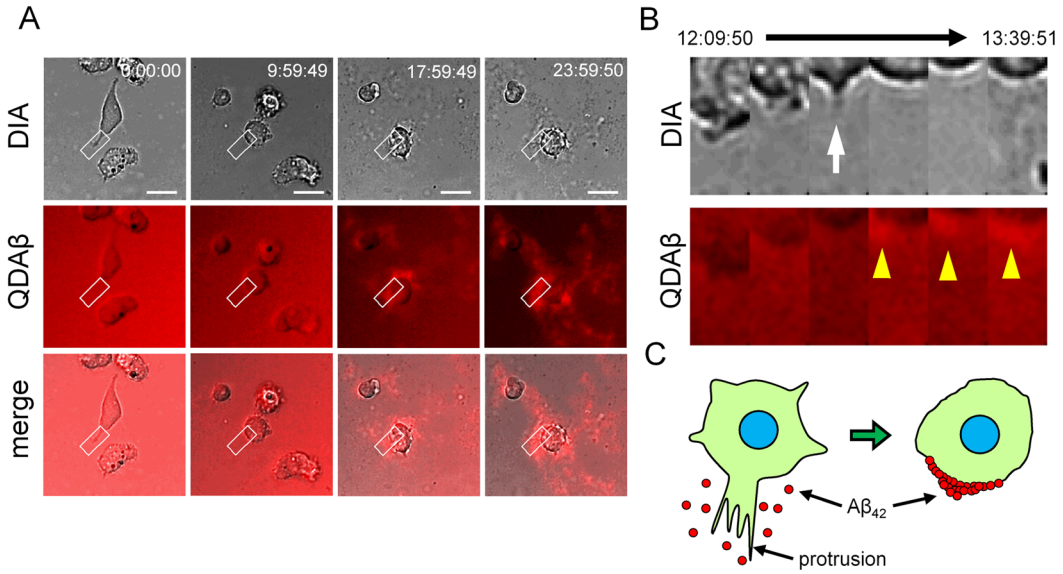

Figure 3. 2D real-time imaging of cell protrusion and $A\beta_{42}$ aggregation. (**A**) PC12 cells were co-incubated with 20 μM $A\beta_{42}$ and 30 nM QDAβ, and observed by a conventional inverted microscope (DIA) and confocal microscope (QDAβ). Time series of images show the gradual steps of $A\beta_{42}$ aggregation at the cell periphery. Bar = 20 μm. (**B**) Kymograph of cell periphery in enlarged image of panel A (white boxes) show that $A\beta_{42}$ starts to aggregate after formation of the protrusion. The cell is localized on the top side of the panel. White arrow and yellow arrowheads indicate membrane protrusion and $A\beta_{42}$ aggregates, respectively. (**C**) Schematic model of the $A\beta_{42}$ aggregation around protrusions of PC12 cells.

(Supplementary Fig. S6). These phenomena are considered to be important processes in the mechanism of cell death caused by $A\beta_{42}$ aggregation. Interestingly, after cell death, $A\beta_{42}$ aggregates, which accumulated on the cell surface, remained there. As shown in Fig. 6 (time point at 11 h 59 min), even after the membrane blebbed and the cytoplasm flowed out, the $A\beta_{42}$ aggregates maintained a rough cell morphology, like a "husk". We suggested the schematic illustration of cell death caused by $A\beta_{42}$ aggregations (Fig. 6C). Furthermore, additional $A\beta_{42}$ aggregation occurred and continued to grow, so the basis of this "husk" consists of $A\beta_{42}$ aggregates (Supplementary Movie S7: time point at 14 h 14 min).

F-actin polymerization enhanced $A\beta_{42}$ aggregation on the cell surface via protrusion regulation. Here, we hypothesized that cytoskeletal actin, which is essential for the control of cell morphology and cell motility, is involved in the mechanism of $A\beta_{42}$ aggregation around cells. To investigate the role of actin in protrusion-dependent $A\beta_{42}$ aggregation, we visualized F-actin of PC12 cells using Alexa 647-phalloidin. $A\beta_{42}$ and F-actin colocalized at the cell periphery (Fig. 7A). Many $A\beta_{42}$ aggregates were localized in the region where F-actin had accumulated. To examine whether actin polymerization avidity in protrusions is necessary for $A\beta_{42}$ aggregation, we inhibited actin polymerization of cells using 20 μg/ml cytochalasin D, which is an actin polymerization inhibitor that caps the barbed end of F-actin[34]. Before the experiment, we analyzed the effect of cytochalasin D on $A\beta_{42}$ aggregation using MSHTS methods[28,29]. In MSHTS method, we quantified the amount of $A\beta_{42}$ aggregates from standard deviation (SD) values of fluorescence intensity of each pixel. Addition of cytochalasin D (0.16-100 μg/ml) did not change the SD value compared to control sample (Supplementary Fig. S7), indicating that $A\beta_{42}$ aggregation was not directly inhibited by 100 μg/ml cytochalasin D. Then, we confirmed that 20 μg/ml of cytochalasin D treatment suppressed $A\beta_{42}$ aggregation around cells (Fig. 7B). These results indicate that the formation of F-actin polymerization-dependent protrusions is required for the preferential aggregation of $A\beta_{42}$ at the cell periphery.

Discussion

In this study, by adding $A\beta_{42}$ and QDAβ to a culture model neuron, we succeeded in real-time imaging of the aggregation process of $A\beta_{42}$ around cells. It was revealed that the aggregation of $A\beta_{42}$ is not uniform on the cell surface and that preferential aggregation is promoted at the cell periphery where cell protrusions are intensely formed. We also demonstrated that actin polymerization-dependent cell motility is responsible for the promotion of $A\beta_{42}$ aggregation at the peripheral region of PC12 cells.

Lu *et al.* reported the gradual aggregation of Aβ that exists inside culture cells and defined the assembly of Aβ fibrils as an aggresome that grows until several micrometers in diameter[10]. Here, we also visualized extracellular aggregation. We confirmed that $A\beta_{42}$ aggregates formed a unit several micrometers in diameter and that these $A\beta_{42}$ units interacted with each other, then aggregated in solution (M. Kuragano *et al.*, manuscript in preparation). It is possible that $A\beta_{42}$ aggregates might exhibit an upper size limit of several micrometers. By using a

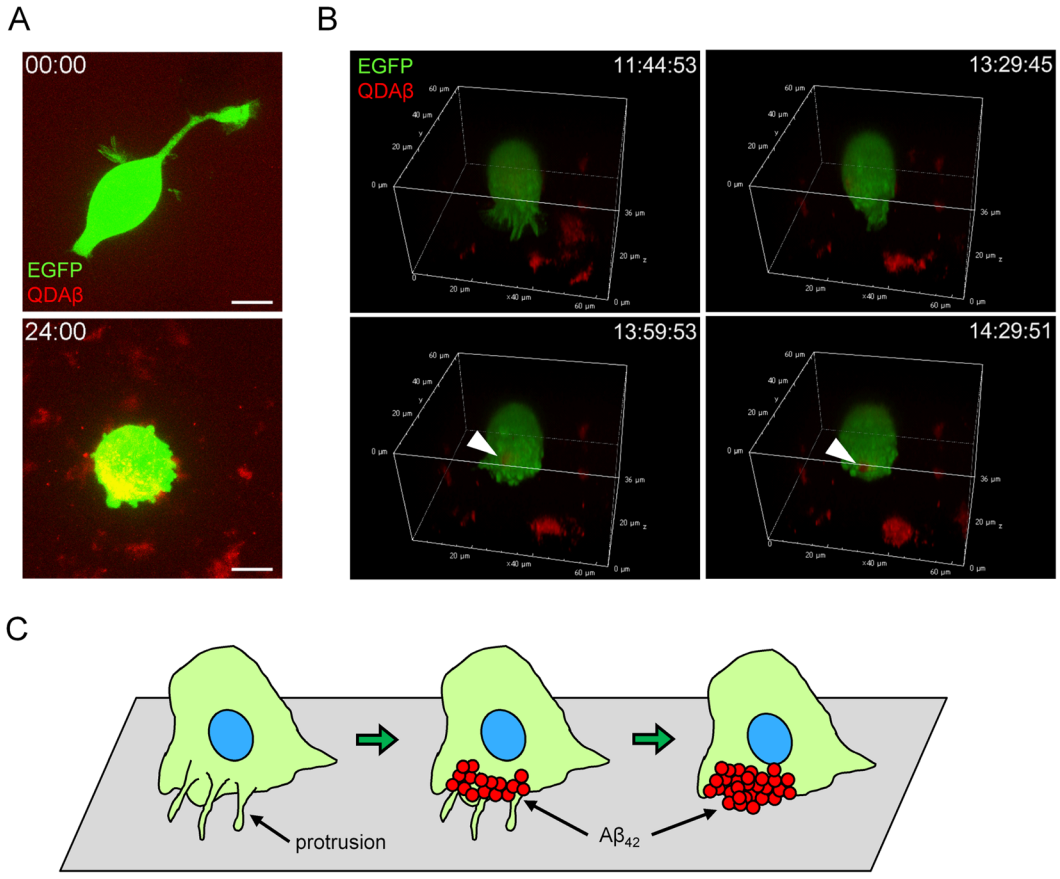

Figure 4. 3D real-time imaging of cell protrusion and $A\beta_{42}$ aggregation. (**A**) Image of maximum fluorescence intensity projection of 0 and 24 h time point in 3D real-time imaging. PC12 cells were co-incubated with 16 μM $A\beta_{42}$ and 30 nM QDAβ. $A\beta_{42}$ aggregates at the cell periphery at the 24 h time point. Bar = 10 μm. (**B**) 3D reconstruction images of Panel (A). Active protrusions formed from the cell surface at 11 h 45 min (upper left). $A\beta_{42}$ started to aggregate in the part indicated by white arrowheads. Images were captured by a confocal microscope. (**C**) Schematic 3D model of the $A\beta_{42}$ aggregation around protrusions of PC12 cells.

super-resolution microscope, new insight about classification of the process of aggregation at the cell periphery might be obtained.

Recently, it was reported that the aggregation of Aβ is promoted under the presence of surfactants, such as micelles, near the cell membrane[16,35]. Wakabayashi *et al.* reported that gangliosides present in sphingolipids and cholesterol-rich domains called "lipid rafts" on cell membranes function as scaffolds for Aβ aggregation[15]. Here, we hypothesized that the diffusion of $A\beta_{42}$ transits from a three-dimensional area in culture medium to a two-dimensional plane on the surface of the cell membrane (Fig. 8A) and that the intense cell membrane protrusions driven by actin polymerization dramatically increase the frequency of collisions among $A\beta_{42}$ molecules at the cell surface (Fig. 8B), which promotes additional $A\beta_{42}$ aggregation. Observation of the maturation of early $A\beta_{42}$ aggregates *in vitro* also supports the possibility that the aggregation nucleus initially formed on the cell surface, incorporated new $A\beta_{42}$, and exhibited the growth of aggregates (Supplementary Fig. S8 and Supplementary Movie S8).

We also showed that $A\beta_{42}$ aggregates at the cell surface can cause cell death. Neuronal death is considered to be triggered by promoting the formation of $A\beta_{42}$ aggregates on the cell membrane. In fact, apoptosis of SH-SY5Y cells, was induced by Aβ fibrillation[33]. After abnormal morphological changes of the cell and nucleus, the cell membrane was disrupted, then neuronal cells died. Moreover, we found that the reduced cell membrane plasticity caused by $A\beta_{42}$ accumulation may be involved in the expression of its neurocytotoxicity[36,37]. Remarkably, $A\beta_{42}$ aggregates on the surface of PC12 cells remained there, even after cell death. After frequent membrane blebbing and spillage of the cellular components due to cell death, the aggregated $A\beta_{42}$ continued to stay in place as if it had left the cell outline. This "husk" also seems to play the function of an aggregation nucleus, i.e., new aggregates accumulated on this "husk". The amyloid cascade hypothesis suggested that the emergence of an amyloid plaque (senile plaque) is major feature of the expression of AD[2]. Although the real-time imaging of plaque formation in local neuronal tissue of transgenic mice was observed using multiphoton microscopy[38], details of the processes and molecular mechanism underlying its formation are still obscure[39]. In addition to the newly formed plaques in the microenvironment near the neuronal cells[38], we hypothesized that $A\beta_{42}$ aggregation remaining around dead cells might mature into amyloid plaques. Actually, it was reported that the size-order of amyloid plaques is about the same as neuronal cells and that amyloid plaques consist of proteins, carbohydrates, nucleic acids, lipids, and

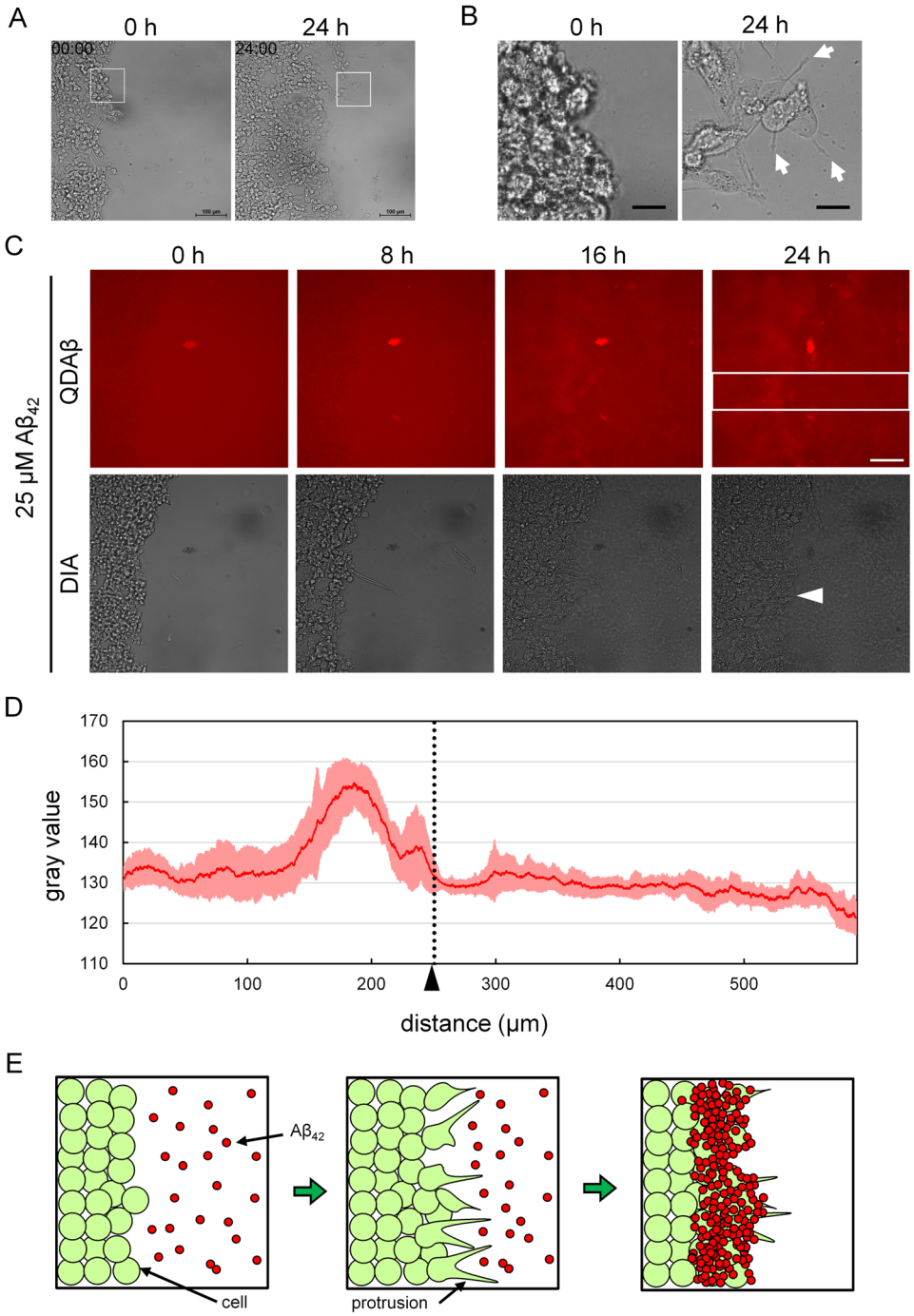

Figure 5. $A\beta_{42}$ aggregation induced at edge of migrating PC12 cells. (**A**) The monolayer of PC12 cells was scratched by toothpick and defined as 0 h. Images of live cell migrated to wounded gap were captured every 10 min for 24 h. Bar = 100 μm. (**B**) Boxed region of panel A. Image of 24 h time point showed that migrating PC12 cells elongated protrusions (white arrows). Bar = 20 μm. (**C**) The monolayer of PC12 cells was scratched by toothpick. Then, PC12 cells were co-incubated with 25 μM $A\beta_{42}$ and 30 nM QDAβ, and observed by a conventional inverted microscope. Time series of images show the gradual steps of cell migration and $A\beta_{42}$ aggregation at wounded edge (white arrowhead). Images of live cell migrated to wounded gap were captured every 10 min for 24 h. Images of QD channel were false-colored in red using image J software. Bar = 100 μm. (**D**) Profile plot of boxed region of Panel (C) (QD channel at 24 h) indicates mean gray value per pixel. Plotted value displays a column average plot in boxed region (red line). The line was represented with error bar means ± SD (pink line). Black arrowhead and black dot line indicate the edge of cell group. (**E**) Schematic model of the $A\beta_{42}$ aggregation at edge of migrating PC12 cells.

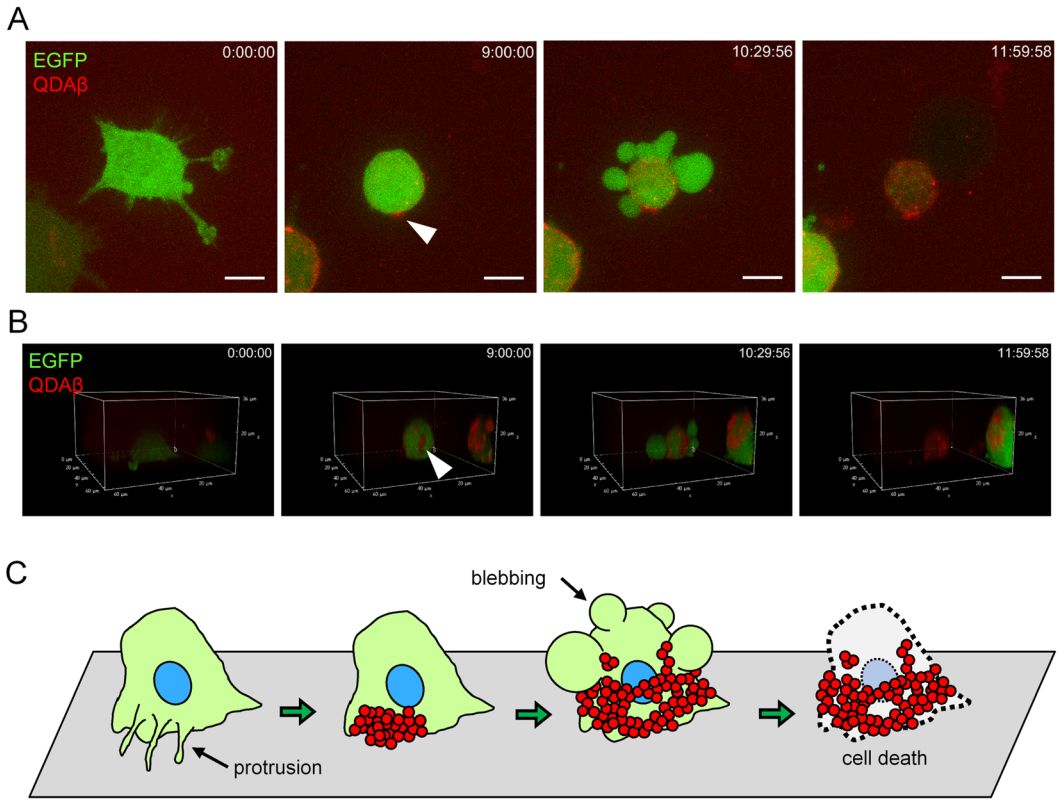

Figure 6. Cell death induced by $A\beta_{42}$ aggregation. (**A**,**B**) Time series images of maximum fluorescence intensity projection (**A**) and images of 3D reconstruction (**B**) of real-time imaging. PC12 cells were co-incubated with 16 μM $A\beta_{42}$ and 30 nM QDAβ. Note that the $A\beta_{42}$-aggregated cell (white arrowheads) exhibited abnormal blebbing and cell death. Images were captured by a confocal microscope. After abnormal blebbing formation, cell death was suddenly induced by $A\beta_{42}$ aggregation. Bars = 10 μm. (**C**) Schematic model of the cell death caused by $A\beta_{42}$ aggregation around PC12 cells.

metal ions[40,41]. Among these major components, lipid rafts on the surface of PC12 cells are known scaffolds of $A\beta_{42}$ aggregation, as mentioned above[15]. It is possible that the debris of dead cells arising from $A\beta_{42}$ neurocytotoxicity accelerate the progression of AD.

F-actin is necessary to regulate neuronal morphology[20] and maintain spine plasticity[42]. SynGAP, a GTPase-activating protein, is the main regulator of actin dynamics of the dendritic spine and is involved with cofilin, which caused disassembly of F-actin by its serving activity[43]. Drebrin is an F-actin-binding protein and is highly expressed in brain tissue[44]. In normal spines, drebrin protects F-actin from serving by cofilin activity. In other words, the drebrin-actin complex exhibits an important function by maintaining spine morphology. Separately, cofilin caused the disappearance of F-actin polymerization in the AD spine[45]. However, we demonstrated that $A\beta_{42}$-treated PC12 cells accumulated F-actin in the cortical region (Fig. 7A). It was reported that cofilin mediated Aβ-induced apoptosis[46]. Our results imply that the cofilin-independent apoptosis pathway was stimulated by the aggregation of $A\beta_{42}$ on the cell surface. In fact, it was reported that F-actin acts as a sensor of apoptosis[47] and that the apoptosis of endothelial cells was caused by stimulation of TNF-α through changes in the actin cytoskeleton and an increase in phosphorylation of the regulatory light chain of non-muscle myosin II[48]. It is possible that $A\beta_{42}$ aggregation directly suppresses flexibility of the cell membrane and decreases cell plasticity. In addition, the F-actin cytoskeletal fractions, which are supposed to be used for cell membrane protrusion, are thought to have nowhere to localize, allowing them to start to accumulate under the membrane. Consequently, the apoptosis pathway might be induced. It is essential to consider in the future whether the excessive accumulation of actin, which is induced by $A\beta_{42}$, may affect myosin II activity. A well-known structure in the brain, the dendritic spine, protrudes from the dendrite of a nerve cell[49]. Changes in the number and shape of these structures, which play a role in receiving information from most excitatory synapses in the brain, are thought to be involved in the mechanism of neuroplasticity[49,50]. Dendritic spines are generally classified into two sizes, small and large spines, which exhibit different properties[50,51]. Particularly, immature small spines, with filopodia-like structures, exhibit more active movement and a shorter lifetime than large spines[49]. As shown in Figs. 3–5, dynamic membrane movement promoted $A\beta_{42}$ aggregation around cells. It is possible that $A\beta_{42}$ aggregation occurred preferentially on the surface of small spines than on large spines in the brain. In other words, it is reasonable to expect that small spines are susceptible to neurocytotoxicity due to $A\beta_{42}$ aggregation. Although large spines have more F-actin than small spines in proportion to their surface area, its motility is lower than that of

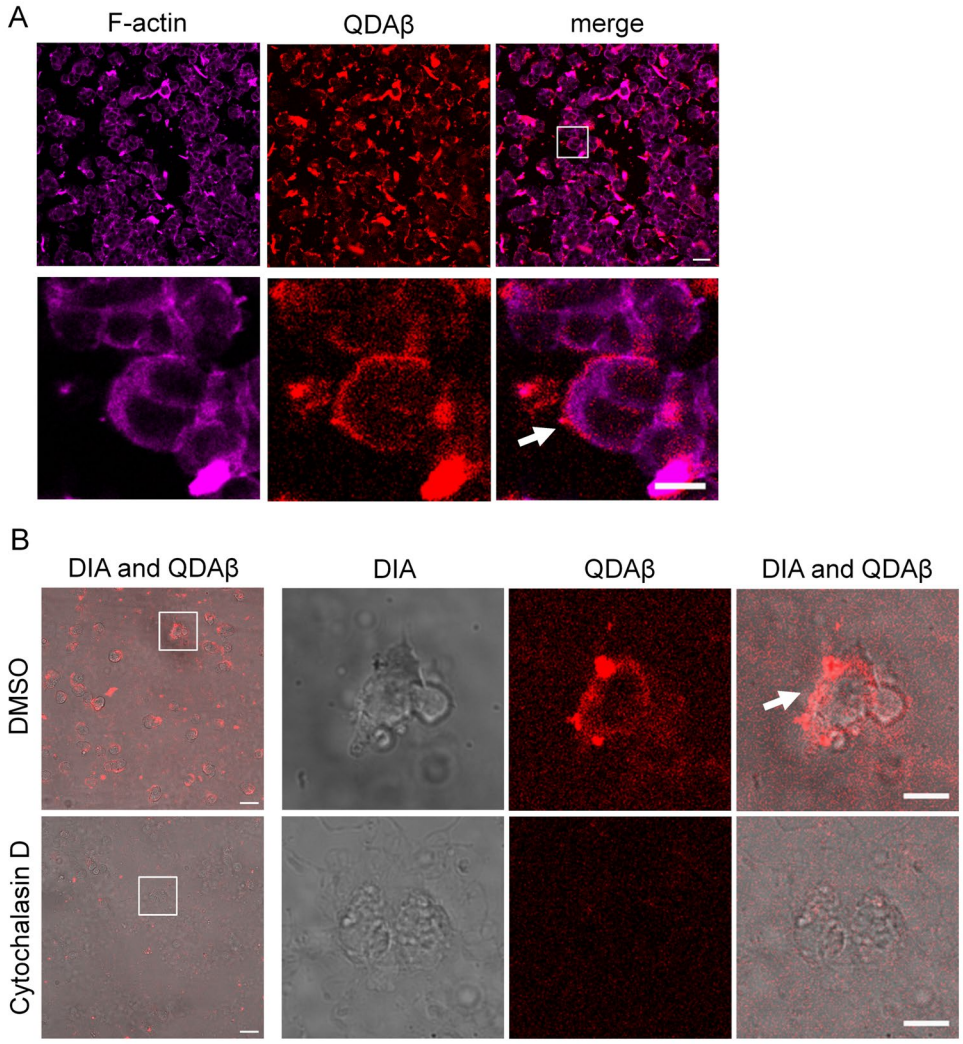

Figure 7. F-actin polymerization-dependent cell membrane movement is required for $A\beta_{42}$ aggregation on the cell surface. (**A**) PC12 cells were co-incubated with 20 μM $A\beta_{42}$ and 30 nM QDAβ (red) for 24 h and were stained with Alexa 647-phalloidin (magenta), and then observed by a confocal microscope. Bar = 50 μm. Bottom panels indicates enlarged images of boxed region in the top panels. Bar = 20 μm. The white arrow points to colocalization of $A\beta_{42}$ aggregates and F-actin accumulation in the cell periphery region. (**B**) PC12 cells were treated with DMSO (control) or 20 μg/ml cytochalasin D for 24 h and then co-incubated with 20 μM $A\beta_{42}$ and 30 nM QDAβ (red) for 24 h. Bar = 50 μm. Images were captured using a confocal microscope (QDAβ) and a conventional inverted microscope (DIA). Right three panels indicate enlarged images of the boxed region in the left panel. Cytochalasin D inhibited $A\beta_{42}$ aggregation at the cell periphery. Bar = 20 μm.

small spines. Currently, we are working on elucidating the molecular mechanism of $A\beta_{42}$ aggregation-dependent cell death through F-actin accumulation.

Materials and Methods

Cell culture. Rat adrenal pheochromocytoma, PC12 cells, were obtained from the JCRB Cell Bank (Japan). Mouse neuroblastoma × rat glioma, NG108-15 cells, were a kind gift by Prof. Hiroyuki Nakagawa (Fukuoka University). PC12 cells were maintained in RPMI (Gibco/Life Technologies, USA) supplemented with 5% fetal bovine serum (FBS) (Gibco/Life Technologies) and 10% horse serum (HS) (Gibco/Life Technologies) or DMEM (Wako, Japan) supplemented with 10% FBS. NG108-15 cells were maintained in DMEM supplemented with 10% FBS. All culture media were supplemented with 100 U/mL penicillin and 100 μg/mL streptomycin (Wako). Cells were cultured at 37 °C in humidified air containing 5% CO_2.

Reagents. Poly-D-Lysine was purchased from Sigma-Aldrich (USA). Human $A\beta_{42}$ (4349-v; Peptide Institute, Japan) and Cys-conjugated $A\beta_{40}$ (23519; Anaspec, USA) were purchased commercially. Nerve growth factor was purchased from Cosmo Bio (Japan). Alexa 647-phalloidin and Hoechst 33342 were purchased from Invitrogen (USA). CellBrite were purchased from Biotium (USA).

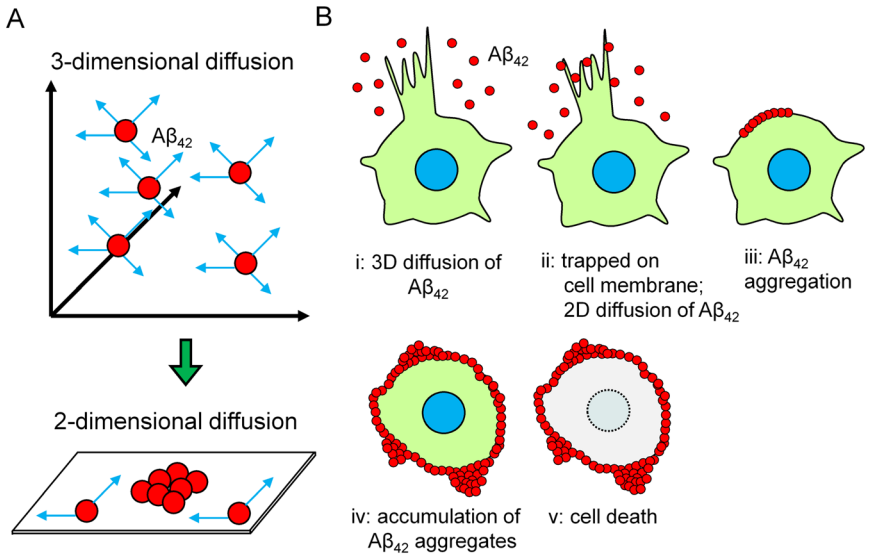

Figure 8. Schematic model of novel $A\beta_{42}$ aggregation process on the cell surface. (**A**) Transition of the $A\beta_{42}$ movement state from three-dimensional to two-dimensional diffusion. Due to the frequency of collisions between each $A\beta_{42}$ monomer on the cell membrane surface, aggregation is thought to increase there. (**B**) Relationship between the formation of cell protrusion and promotion of $A\beta_{42}$ aggregation. The frequency of collisions between each $A\beta_{42}$ monomer on the cell membrane might increase in the area where active protrusions formed, more than in the static region. Therefore, it is thought that $A\beta_{42}$ aggregate formation is particularly promoted at the cell edge where movement is active.

Preparation of QDAβ nanoprobes. QDAβ nanoprobe was prepared using QD-PEG-NH_2 (Qdot 655 ITK Amino (PEG) Quantum dot; Q21521MP or Qdot 605 ITK Amino (PEG) Quantum dot; Q21501MP, Thermo Fisher Scientific, USA) according to our previous reports[28–30]. The QDAβ nanoprobe was prepared as follows: 10 μM QD-PEG-NH_2 was first reacted with 1 mM sulfo-EMCS (22307; Pierce/Thermo Fisher Scientific) in PBS for 1 h at room temperature. After quenching and eliminating unreacted sulfo-EMCS, the QD-PEG-NH_2-bound sulfo-EMCS was reacted with 74 μM Cys-conjugated $A\beta_{40}$ for 1 h at room temperature. The concentration of QDAβ was determined by comparing absorbance at 350 nm to unlabeled QD-PEG-NH_2.

MSHTS system. The SD values in existence of cytochalasin D were determined by a modified MSHTS system, as was described in our previous reports[28–30]. More specifically, various concentrations of cytochalasin D, 25 μM $A\beta_{42}$ and 25 nM QDAβ in PBS were incubated in a 1536-well plate (782096, Greiner Bio-One, Austria) at 37 °C for 24 h. The QDAβ-$A\beta_{42}$ aggregates that formed in each well were observed by an inverted fluorescence microscope (TE2000, Nikon) equipped with a color CCD camera (DP72, Olympus) and an objective lens (Plan Fluor 4×/0.13 PhL DL, Nikon). SD values of fluorescence intensities of 40,000 pixels (200 × 200 pixels) around the central region of each well were measured by Image J software (NIH, USA).

MTT assay. PC12 cells were plated at 2.0×10^4 cells in poly-D-lysine-coated 96-well plates (IWAKI, Japan) and incubated for 24 h. After incubation, cells were treated with 4.5 ng/ml NGF and further incubated for 24 h. Then, cells were treated with QD, QDAβ, and $A\beta_{42}$ and cells were incubated for a further 24 h. Then, cells were treated with 1.2 mM MTT and incubated for 4 h. After incubation, the supernatant of each well was removed and then crystals of formazan were dissolved in 10% SDS/0.01 M HCl solution. After overnight incubation, absorbance intensity (570 nm) was measured in a 96-well plate. Cell viability was assessed as a percentage relative to DMSO-treated cells.

Transfection. pEGFP was a kind gift from Assoc. Prof. Masayuki Takahashi (Hokkaido University). Cells were transfected with plasmid DNA using Superfect Transfection Reagent (Qiagen, Germany) in DMEM according to the manufacturer's protocol. Transfected cells were replated onto a glass-bottom 96-well plate (Corning, USA) precoated with 0.1 mg/mL poly-D-lysine for live cell imaging.

time-lapse observation. For single cell motility observation, time-lapse images were captured with an inverted microscope (Ti-E; Nikon, Japan) equipped with a color CMOS camera (DS-Ri2; Nikon) and an objective lens (PlanApo λ 20×/0.75 NA; Nikon). During observation, the cells were maintained in DMEM/F12 (1:1) (Gibco/Life Technologies) supplemented with 10% FBS and warmed in a chamber set at 37 °C. Images were captured every 10 min and analyzed using NIS-Elements C software (Nikon). For WHA, PC12 cells were plated at 10×10^4 cells in a glass-bottom 96-well plate precoated with 0.1 mg/mL poly-D-lysine. Cells were incubated for 24 h. After incubation, cells were treated with 45 ng/ml NGF and further incubated for 24 h. Then, after removal of culture medium, cell monolayer was scratched by toothpick and defined as 0 h. Then, the wells were filled by

DMEM/F12 (1:1) supplemented with 10% FBS and 45 ng/ml NGF. This new medium included 1% DMSO or 25 μM $A\beta_{42}$ and 30 nM QDAβ. Time lapse observations were performed in the same way as above described. Fluorescence images were captured as 8-bit grayscale images. All images were adjusted by a macro program so that average intensity became 50% according to our previous report method[29]. The mean gray value per pixel of $A\beta_{42}$ aggregates was measured by the plot profile, the function of Image J software.

Confocal laser scanning microscopy. Z-stacks images were captured using an inverted microscope (Ti-E) and a confocal laser microscope system (C2 Plus; Nikon) equipped with an objective lens (PlanApo λ 20×/0.75 NA; Nikon, Plan Apo λ 100×/1.45 NA Oil; Nikon). Cells were maintained in RPMI supplemented with 5% FBS and 10% HS and warmed in a chamber set at 37 °C (INUBTF-WSKM-B13I; Tokai Hit) during observation. Images were captured and analyzed using NIS-Elements C software. For 3D time-lapse imaging, cells were maintained in DMEM/F12 (1:1) supplemented with 10% FBS and 4.5 ng/ml NGF, and warmed in a chamber set at 37 °C during observation. EGFP and QD were excited by a laser at 488 and 561 nm, respectively. Z-stack images were captured every 15 min and were oversampled by taking 1000 nm z-steps between acquired images and were analyzed using NIS-Elements C software. For observation of $A\beta_{42}$ aggregation by the MSHTS system, 25 μM $A\beta_{42}$ in and 25 nM QDAβ, PBS containing 5% EtOH and 3% DMSO were incubated in a 1536-well plate (782096; Greiner) warmed in a chamber set at 37 °C. Z-stack images were captured every 3 min and were oversampled by taking 2500 nm z-steps between acquired images and were analyzed using NIS-Elements C software.

Received: 25 December 2019; Accepted: 13 May 2020;
Published online: 16 June 2020

References

1. Lane, C. A., Hardy, J. & Schott, J. M. Alzheimer's disease. *Eur. J. Neurol.* **25**, 59–70 (2018).
2. Hardy, J. & Selkoe, D. J. The amyloid hypothesis of Alzheimer's disease: progress and problems on the road to therapeutics. *Science* **297**, 353–356 (2002).
3. Scheltens, P. *et al*. Alzheimer's disease. *Lancet* **388**, 505–517 (2016).
4. Koo, E. H., Lansbury, P. T. & Kelly, J. W. Amyloid diseases: abnormal protein aggregation in neurodegeneration. *Proc. Natl. Acad. Sci. USA* **96**, 9989–90 (1999).
5. Walsh, D. M., Lomakin, A., Benedek, G. B., Condron, M. M. & Teplow, D. B. Amyloid beta-protein fibrillogenesis. Detection of a protofibrillar intermediate. *J. Biol. Chem.* **272**, 22364–72 (1997).
6. Walsh, D. M. *et al*. Amyloid beta-protein fibrillogenesis. Structure and biological activity of protofibrillar intermediates. *J. Biol. Chem.* **274**, 25945–52 (1999).
7. Malinchik, S. B., Inouye, H., Szumowski, K. E. & Kirschner, D. A. Structural analysis of Alzheimer's beta(1-40) amyloid: protofilament assembly of tubular fibrils. *Biophys. J.* **74**, 537–45 (1998).
8. Harris, J. R. *In vitro* fibrillogenesis of the amyloid beta 1-42 peptide: cholesterol potentiation and aspirin inhibition. *Micron* **33**, 609–26 (2002).
9. Querol-Vilaseca, M. *et al*. Nanoscale structure of amyloid-β plaques in Alzheimer's disease. *Sci. Rep.* **9**, 5181 (2019).
10. Lu, M. *et al*. Structural progression of amyloid-β Arctic mutant aggregation in cells revealed by multiparametric imaging. *J. Biol. Chem.* **294**, 1478–1487 (2019).
11. McLaurin, J., Yang, D. S., Yip, C. M. & Fraser, P. E. Review: Modulating factors in amyloid-β fibril formation. *J. Struct. Biol.* **130**, 259–270 (2000).
12. Gorbenko, G. P. & Kinnunen, P. K. J. The role of lipid-protein interactions in amyloid-type protein fibril formation. *Chem. Phys. Lipids* **141**, 72–82 (2006).
13. Yip, C. M., Darabie, A. A. & McLaurin, J. A. Aβ42-peptide assembly on lipid bilayers. *J. Mol. Biol.* **318**, 97–107 (2002).
14. Yamaguchi, H. *et al*. Amyloid β protein (Aβ) starts to deposit as plasma membrane-bound form in diffuse plaques of brains from hereditary cerebral hemorrhage with amyloidosis-Dutch type, Alzheimer disease and nondemented aged subjects. *J. Neuropathol. Exp. Neurol.* **59**, 723–732 (2000).
15. Wakabayashi, M. & Matsuzaki, K. Formation of Amyloids by Aβ-(1-42) on NGF-differentiated PC12 Cells: Roles of Gangliosides and Cholesterol. *J. Mol. Biol.* **371**, 924–933 (2007).
16. Han, S. *et al*. Amyloid plaque structure and cell surface interactions of β-amyloid fibrils revealed by electron tomography. *Sci. Rep.* **7**, 43577 (2017).
17. Sugiura, Y., Ikeda, K. & Nakano, M. High Membrane Curvature Enhances Binding, Conformational Changes, and Fibrillation of Amyloid-β on Lipid Bilayer Surfaces. *Langmuir* **31**, 11549–11557 (2015).
18. Terakawa, M. S., Yagi, H., Adachi, M., Lee, Y. H. & Goto, Y. Small liposomes accelerate the fibrillation of amyloid β(1- 40). *J. Biol. Chem.* **290**, 815–826 (2015).
19. Mitchison, T. J. & Cramer, L. P. Actin-based cell motility and cell locomotion. *Cell* **84**, 371–379 (1996).
20. Penzes, P. & Rafalovich, I. Regulation of the actin cytoskeleton in dendritic spines. *Adv. Exp. Med. Biol.* **970**, 81–95 (2012).
21. Honkura, N., Matsuzaki, M., Noguchi, J., Ellis-Davies, G. C. R. R. & Kasai, H. The subspine organization of actin fibers regulates the structure and plasticity of dendritic spines. *Neuron* **57**, 719–729 (2008).
22. Nakayama, A. Y., Harms, M. B. & Luo, L. Small GTPases Rac and Rho in the maintenance of dendritic spines and branches in hippocampal pyramidal neurons. *J. Neurosci.* **20**, 5329–5338 (2000).
23. Penzes, P. *et al*. Rapid induction of dendritic spine morphogenesis by trans-synaptic ephrinB-EphB receptor activation of the Rho-GEF kalirin. *Neuron* **37**, 263–274 (2003).
24. Tashiro, A., Minden, A. & Yuste, R. Regulation of dendritic spine morphology by the rho family of small GTPases: antagonistic roles of Rac and Rho. *Cereb. Cortex* **10**, 927–938 (2000).
25. Kommaddi, R. P. *et al*. Aβ mediates F-actin disassembly in dendritic spines leading to cognitive deficits in Alzheimer's disease. *J. Neurosci.* **38**, 1085–1099 (2018).
26. Henriques, A. G., Oliveira, J. M., Carvalho, L. P. & da Cruz e Silva, O. A. B. B. Aβ Influences Cytoskeletal Signaling Cascades with Consequences to Alzheimer's Disease. *Mol. Neurobiol.* **52**, 1391–1407 (2015).
27. Tokuraku, K., Marquardt, M. & Ikezu, T. Real-Time Imaging and Quantification of Amyloid-β Peptide Aggregates by Novel Quantum-Dot Nanoprobes. *PLoS One* **4**, e8492 (2009).
28. Ishigaki, Y. *et al*. A microliter-scale high-throughput screening system with quantum-dot nanoprobes for amyloid-β aggregation inhibitors. *PLoS One* **8**, e72992 (2013).
29. Sasaki, R. *et al*. An automated microliter-scale high-throughput screening system (MSHTS) for real-time monitoring of protein aggregation using quantum-dot nanoprobes. *Sci. Rep.* **9**, 2587 (2019).

30. Ogara, T., Takahashi, T., Yasui, H., Uwai, K. & Tokuraku, K. Evaluation of the effects of amyloid b aggregation from seaweed extracts by a microliter-scale high-throughput screening system with a quantum dot nanoprobe. *J. Biosci. Bioeng.* **120**, 45–50 (2015).
31. Liang, C.-C., Park, A. Y. & Guan, J.-L. *In vitro* scratch assay: a convenient and inexpensive method for analysis of cell migration *in vitro*. *Nat. Protoc.* **2**, 329–333 (2007).
32. Wu, C.-L. *et al*. Interplay between cell migration and neurite outgrowth determines SH2B1β-enhanced neurite regeneration of differentiated PC12 cells. *PLoS One* **7**, e34999 (2012).
33. Krishtal, J., Bragina, O., Metsla, K., Palumaa, P. & Tõugu, V. *In situ* fibrillizing amyloid-beta 1-42 induces neurite degeneration and apoptosis of differentiated SH-SY5Y cells. *PLoS One* **12**, e0186636 (2017).
34. Carlier, M. F., Criquet, P., Pantaloni, D. & Korn, E. D. Interaction of cytochalasin D with actin filaments in the presence of ADP and ATP. *J. Biol. Chem.* **261**, 2041–2050 (1986).
35. Soreghan, B., Kosmoski, J. & Glabe, C. Surfactant properties of Alzheimer's A beta peptides and the mechanism of amyloid aggregation. *J. Biol. Chem.* **269**, 28551–28554 (1994).
36. Li, Y. *et al*. Role of amyloid β protein receptors in mediating synaptic plasticity. *Biomed. reports* **6**, 379–386 (2017).
37. Rowan, M. J., Klyubin, I., Wang, Q. & Anwyl, R. Synaptic plasticity disruption by amyloid beta protein: modulation by potential Alzheimer's disease modifying therapies. *Biochem. Soc. Trans.* **33**, 563–567 (2005).
38. Meyer-Luehmann, M. *et al*. Rapid appearance and local toxicity of amyloid-beta plaques in a mouse model of Alzheimer's disease. *Nature* **451**, 720–724 (2008).
39. Takahashi, R. H., Nagao, T. & Gouras, G. K. Plaque formation and the intraneuronal accumulation of β-amyloid in Alzheimer's disease. *Pathol. Int.* **67**, 185–193 (2017).
40. Stewart, K. L. & Radford, S. E. Amyloid plaques beyond Aβ: a survey of the diverse modulators of amyloid aggregation. *Biophys. Rev.* **9**, 405–419 (2017).
41. Liao, L. *et al*. Proteomic characterization of postmortem amyloid plaques isolated by laser capture microdissection. *J. Biol. Chem.* **279**, 37061–37068 (2004).
42. Fischer, M., Kaech, S., Knutti, D. & Matus, A. Rapid actin-based plasticity in dendritic spines. *Neuron* **20**, 847–854 (1998).
43. Carlisle, H. J., Manzerra, P., Marcora, E. & Kennedy, M. B. SynGAP regulates steady-state and activity-dependent phosphorylation of cofilin. *J. Neurosci.* **28**, 13673–13683 (2008).
44. Hayashi, K. *et al*. Modulatory role of drebrin on the cytoskeleton within dendritic spines in the rat cerebral cortex. *J. Neurosci.* **16**, 7161–7170 (1996).
45. Kojima, N. & Shirao, T. Synaptic dysfunction and disruption of postsynaptic drebrin-actin complex: a study of neurological disorders accompanied by cognitive deficits. *Neurosci. Res.* **58**, 1–5 (2007).
46. Bamburg, J. R. & Bernstein, B. W. Actin dynamics and cofilin-actin rods in alzheimer disease. *Cytoskeleton (Hoboken).* **73**, 477–497 (2016).
47. Desouza, M., Gunning, P. W. & Stehn, J. R. The actin cytoskeleton as a sensor and mediator of apoptosis. *Bioarchitecture* **2**, 75–87 (2012).
48. Petrache, I. *et al*. Differential effect of MLC kinase in TNF-alpha-induced endothelial cell apoptosis and barrier dysfunction. *Am. J. Physiol. Lung Cell. Mol. Physiol.* **280**, 1168–1178 (2001).
49. Berry, K. P. & Nedivi, E. Spine Dynamics: Are They All the Same? *Neuron* **96**, 43–55 (2017).
50. Matsuzaki, M., Honkura, N., Ellis-Davies, G. C. R. & Kasai, H. Structural basis of long-term potentiation in single dendritic spines. *Nature* **429**, 761–766 (2004).
51. Paulin, J. J. W. *et al*. Large and Small Dendritic Spines Serve Different Interacting Functions in Hippocampal Synaptic Plasticity and Homeostasis. *Neural Plast.* **2016**, 6170509 (2016).

Acknowledgements

This work was supported by JSPS KAKENHI Grant Number JP25350974, 16K14704, and JP16H03288 (K.T.). We are grateful to Assoc. Prof. Masayuki Takahashi (Hokkaido University) for helpful discussion.

Author contributions

M.K. wrote the paper, and performed experimental work and data analysis on 3D real time imaging of cells and $A\beta_{42}$ aggregation. R.Y. performed experimental work and data analysis on major parts. Y.C. performed experimental work and data analysis on 2D real time imaging. R.K. performed WHA and analysis. K.T. designed the project, performed the experimental work, data analysis, and wrote the paper.

Competing interests

We declare that the authors have no competing interests as defined by Nature Research, or other interests that might be perceived to influence the results and/or discussion reported in this paper.

Additional information

Supplementary information is available for this paper at https://doi.org/10.1038/s41598-020-66129-z.

Correspondence and requests for materials should be addressed to K.T.

Reprints and permissions information is available at www.nature.com/reprints.

Publisher's note Springer Nature remains neutral with regard to jurisdictional claims in published maps and institutional affiliations.